

Structural evolution of Bi thin films on Au(111) revealed by scanning tunneling microscopyNaoya Kawakami,¹ Chun-Liang Lin,¹ Kazuaki Kawahara,¹ Maki Kawai,^{1,*} Ryuichi Arafune,² and Noriaki Takagi¹¹*Department of Advanced Materials Science, Graduate School of Frontier Science, University of Tokyo, Kashiwa 5-1-5, Chiba 277-8561, Japan*²*International Center for Materials Nanoarchitectonics (WPI-MANA), National Institute for Materials Science, 1-1 Namiki, Ibaraki 305-0044, Japan*

(Received 27 June 2017; revised manuscript received 14 September 2017; published 1 November 2017)

We present the structural evolution of Bi on Au(111) from monolayer to multilayer regimes explored mainly by scanning tunneling microscopy. At the monolayer regime, Bi clusters distribute homogeneously to make an array with 5×5 periodicity. Further increase of the coverage converts these clusters to the two-dimensional periodic $(\sqrt{37} \times \sqrt{37})R25.3^\circ$ and $(p \times \sqrt{3})$ structures. We propose a model of the $(\sqrt{37} \times \sqrt{37})R25.3^\circ$ structure based on the STM measurements and density-functional theory calculations. In the multilayer regime, superstructures at first appear with long-range periodicities arising from the moiré structures due mainly to the stacking of Bi layers. Then, the thicker films grow whose lattice constants are close to those of the (110) surface of rhombohedral Bi crystal. The Bi(110) films of more than 60 layers grow stably. Thus, this system provides a good stage for further investigation of the peculiar electronic properties of Bi(110).

DOI: [10.1103/PhysRevB.96.205402](https://doi.org/10.1103/PhysRevB.96.205402)**I. INTRODUCTION**

Bismuth nanostructures have attracted much attention from both fundamental and application points of view. Large spin-orbit interaction (SOI) of Bi combined with the broken symmetry at the solid surface gives rise to intriguing electronic structures. Large spin splitting, known as Rashba-Bychkov splitting, occurs in the electronic bands of surface alloys formed by the adsorption of Bi on the (111) surfaces of Ag [1] and Cu [2]. The two-dimensional (2D) lattice of Bi can become a 2D topological insulator hosting nontrivial edge states [3–12], and thus Bi(111) and Bi(110) thin films have been investigated (we use rhombohedral notation for describing the Bi surface hereafter). The Bi(110) surface is also worthy of being noticed. The dangling bonds at the surface strongly affect the atomic and electronic structures. In particular, the electronic structure depends on the number of atomic layers: the dangling bonds are saturated only at even-numbered atomic films, while the bonds on the surface of odd-numbered films construct a Dirac cone feature [13]. In addition to these characteristics, recent studies demonstrate that the Bi nanostructures formed on Au and carbon electrodes by electrochemical deposition in aqueous conditions enhance the catalytic activities of the electrodes [14–17]. These novel characteristics promote basic research about the structural evolution of Bi films on solid substrates [18–26].

Coinage metals are often used as a template for synthesizing thin films because of their feasibility. In particular, Au(111) provides a unique template because the surface is reconstructed into a herringbone structure. The structural evolution and electronic properties of Bi on the (111) surface of Cu and Ag have already been reported [1,2,23–27]. In contrast, there are only a few studies concerning the adsorption of Bi on Au(111) under ultrahigh-vacuum (UHV) conditions [28]. Jeon *et al.* [28] investigated the monolayer of Bi on Au(111) by

using scanning tunneling microscopy (STM). They found a well-ordered (6×6) structure and proposed a structural model that consists of the corner hole, Bi adatoms, and stacking faults. Chen *et al.* studied the structure of Bi thin films on Au(111) grown by electrochemical deposition under an aqueous condition [29]. They found that the Bi atoms form (2×2) and $(p \times \sqrt{3})$ periodic structures on Au(111). Although these works provide important results about the structures of Bi thin films on Au(111), there still remains a lot to be elucidated about the structure evolution of Bi on Au(111) from the initial growth to the thick films.

In this paper, we report on the structural evolution of Bi on Au(111) as a function of Bi coverage by using STM. Increasing the coverage in the monolayer regime, the surface structure evolves from a lattice consisting of Bi clusters to $(p \times \sqrt{3})$ through $(\sqrt{37} \times \sqrt{37})R25.3^\circ$. We show through detailed STM measurements that the ordered structure assigned to (6×6) in the previous STM study should be assigned to $(\sqrt{37} \times \sqrt{37})R25.3^\circ$, and we propose a structural model with a combination of STM and density-functional theory (DFT) calculations. In the multilayer regime, Bi(110) thin films form and exhibit various long-range periodicities arising from the moiré interaction. The Bi(110) structure grows stably up to more than 60 layers and changes to Bi(111) by annealing at 470 K.

II. METHODS

All STM experiments were performed under UHV conditions with the base pressure below 2.0×10^{-10} Torr. A single-crystal Au(111) surface was cleaned with several cycles of Ar⁺ sputtering and annealing at 770 K and was used as a substrate for the growth of Bi films. Bi atoms were deposited onto the Au(111) substrate kept at room temperature (RT) by heating a cell of Bi (99.999% purity). The surface coverage of Bi (denoted as θ hereafter) was controlled by the deposition time. The deposition rate was calibrated to be 0.06 ± 0.02 monolayer (ML)/min by observing the structural transition of Bi on Si(111) with reflection high-energy electron

*Present address: Institute for Molecular Science, 38 Nishigo-naka, Myodaiji, Okazaki, 444-8585, Japan.

diffraction. Here, we define 1 ML as 9.3×10^{14} atoms/cm² based on the atom density of Bi(110). Differential conductance (dI/dV) spectra were measured with a lock-in technique in which a sinusoidal modulation voltage of 10 mV at 463.7 Hz was added to the sample voltage. All STM measurements were performed at 4.7 K.

To determine the model of the $(\sqrt{37} \times \sqrt{37})R25.3^\circ$ structure described later, the DFT calculations were performed with the plane-wave-based Vienna Ab Initio Simulation Package (VASP) [30,31] with the projector-augmented wave (PAW) potentials within the generalized gradient approximation (GGA) method [32]. The Perdew-Burke-Ernzerhof (PBE) exchange-correlation functional was used [33]. The kinetic-energy cutoff for the plane-wave basis set was 400 eV. The spin-orbit coupling implemented within VASP was taken into account [34]. The supercell consists of a Bi layer with a vacuum on a four-layer Au slab ~ 16 Å thick along the surface normal and is composed of 148 Au and 18 Bi atoms. The atoms in the bottom layer were fixed at their ideal bulk positions during the structure optimization. The positions of Bi atoms and the top three layers of the Au slab were optimized without any constraint until the forces on individual atoms were less than 0.01 eV/Å. In the self-consistent total energy calculations, the Brillouin zone was sampled with $5 \times 5 \times 1$ k -points.

III. RESULTS AND DISCUSSION

A. Structure evolution of $\theta < 1.0$ ML

Figure 1 shows the structure evolution of Bi on Au(111) as a function of θ . Before the deposition of Bi, the herringbone reconstruction of Au(111) is clearly observed as shown in Fig. 1(a), confirming that a clean and well-defined substrate is prepared. At $\theta = 0.6$ ML, the herringbone structure disappears and many small protrusions appear instead as shown in Fig. 1(b). These protrusions are Bi clusters. With increasing θ , the clusters become closely packed. As Fig. 1(f) shows, diffuse spots emerge in the Fourier-transformed (FT) image. The FT image reflects the surface periodic structure in the same way as low-energy electron diffraction. These spots indicate that the clusters distribute homogeneously to make a hexagonal array. From the distances between the spots in the FT image, the average distance between the clusters is determined to be 1.42 nm, which matches five times the lattice constant of Au(111) (0.288 nm).

The cluster array converts into a periodic structure with the increase of θ . Figure 1(c) shows the STM image of a transition regime in which the cluster array coexists with a periodic structure of the sixfold symmetry. Increasing θ from 0.6 to 0.7 ML, the Bi clusters disappear completely and two periodic structures of six- and twofold symmetries cover the surface as shown in Fig. 1(d). The former structure is identical to one that was reported as (6×6) in the previous STM study [28]. The latter is a stripe structure assigned as $(p \times \sqrt{3})$ in the previous studies about the Bi deposition on Au(111) in the aqueous condition [36,37]. At $\theta = 0.8$ ML, the sixfold structure disappears and the surface is covered with the stripe structure as shown in Fig. 1(e).

STM imaging with high resolution provides the atomic arrangement of the sixfold structure by combining DFT

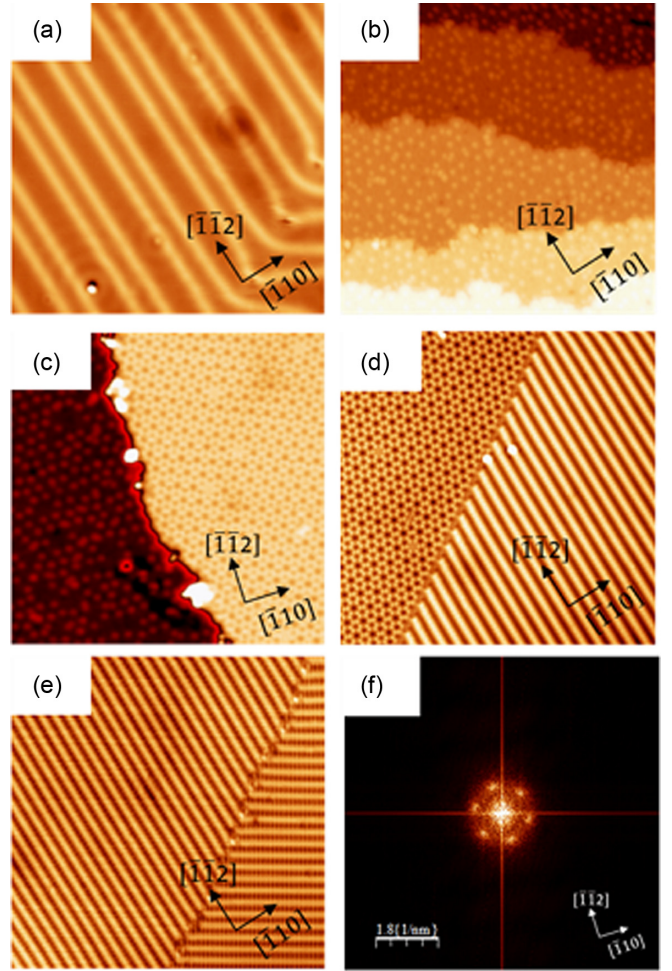


FIG. 1. Structural evolution of Bi on Au(111) below 1 ML. (a) STM image of the clean Au(111) (34×34 nm², $V = 100$ mV, $I = 1.0$ nA). STM images of 34×34 nm² area taken at (b) 0.6 ML ($V = 500$ mV, $I = 1.0$ nA), (c) 0.6 \sim 0.7 ML ($V = 510$ mV, $I = 0.5$ nA), (d) 0.7 ML ($V = 500$ mV, $I = 1.0$ nA), and (e) 0.8 ML ($V = -500$ mV, $I = 1.0$ nA). The crystallographic orientations of the Au(111) substrate are shown in each STM image. The STM images are processed with WSxM [35]. (f) Fourier-transformed image of the region covered with the Bi clusters. Crystallographic orientations of the Au(111) substrate in real space are shown in the lower right corner.

calculations. Figure 2(a) shows an atom-resolved STM image of the sixfold structure. The STM image indicates that the lattice constant is 1.74 nm and that the unit cell rotates by 25° with respect to the Au(111) lattice. Thus, the sixfold structure is assigned to be $(\sqrt{37} \times \sqrt{37})R25.3^\circ$ as in the schematic image shown in Fig. 2(b). This disagrees with the results of the previous STM study in which the sixfold structure is assigned to be (6×6) [28]. Although the lattice constants of these two structures are very close to each other, the difference in angles with respect to the Au(111) lattice brings us to the conclusion that the sixfold structure should be assigned as $(\sqrt{37} \times \sqrt{37})R25.3^\circ$. Furthermore, our assignment is supported by the angle of the sixfold structure relative to the stripe structure. The unit cell of the sixfold

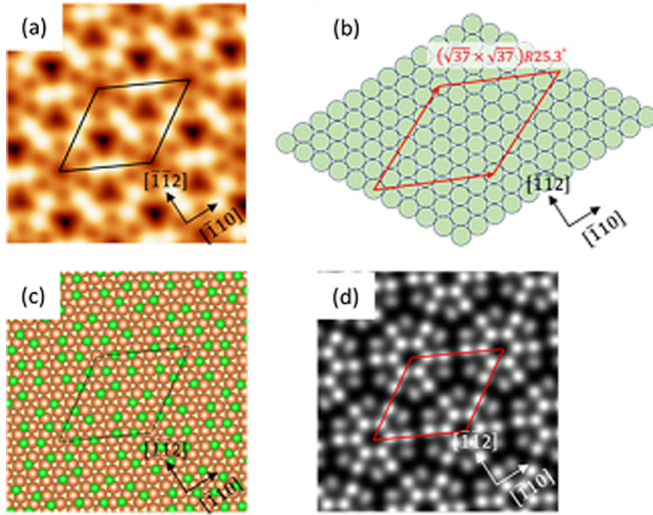


FIG. 2. (a) Atom-resolved STM image of the $(\sqrt{37} \times \sqrt{37})R25.3^\circ$ structure ($5.6 \times 5.6 \text{ nm}^2$, $V = 10 \text{ mV}$, $I = 1.0 \text{ nA}$). (b) Schematic illustration of the Au(111) lattice and the unit cell of the $(\sqrt{37} \times \sqrt{37})R25.3^\circ$ structure. The spheres are Au atoms. (c) Structural model optimized with the DFT calculations. Orange and green spheres represent the Au and Bi atoms, respectively. (d) Simulated STM image at $V = -500 \text{ mV}$. The rhombuses in (a)-(d) indicate the $(\sqrt{37} \times \sqrt{37})R25.3^\circ$ unit cell. The crystallographic orientations of the Au(111) substrate are also shown in (a)-(d).

structure rotates by about 5° with respect to the stripe direction as shown in Fig. 1(d).

We have constructed a $(\sqrt{37} \times \sqrt{37})R25.3^\circ$ structural model by using DFT calculations. Figure 2(c) shows the structural model. The model is developed by considering the protrusions in the STM image as Bi atoms. This model consisting of 18 Bi atoms in the unit cell corresponds to $\theta = 0.73 \text{ ML}$, which reasonably coincides with the range of θ in which the $(\sqrt{37} \times \sqrt{37})R25.3^\circ$ structure is observed experimentally. All the Bi atoms are located at the three-fold hollow site of the unreconstructed Au(111) surface. Figure 2(d) shows an STM image simulated by the DFT calculations. The simulated image reasonably reproduces the features of the experimental image: the corner hole and bridge structure connect two corner holes. Although the relative brightness of the Bi atoms in the simulated image does not match well with the experimental image, we believe that the structural model reasonably describes the atomic arrangement of the $(\sqrt{37} \times \sqrt{37})R25.3^\circ$ structure.

The distance between the stripes in the $(p \times \sqrt{3})$ structure changes slightly with θ . Figures 3(a) and 3(b) show the high-resolution STM images of the stripe structure at $\theta = 0.7$ and 0.8 ML , respectively. A careful analysis reveals that the distance between the neighboring stripes changes from 1.43 nm at 0.7 ML to 1.24 nm at 0.8 ML . This also means that the lattice constant along the direction perpendicular to the stripe depends on θ : 0.48 and 0.47 nm at 0.7 and 0.8 ML , respectively. In contrast, the lattice constant along the stripe is independent of θ . At 0.7 ML , Bi atoms form a commensurate structure described as $(\begin{smallmatrix} \sqrt{3} & 0 \\ 1 & 2 \end{smallmatrix})$, which becomes incommensurate as θ increases to 0.8 ML . The positions of Bi atoms are shown

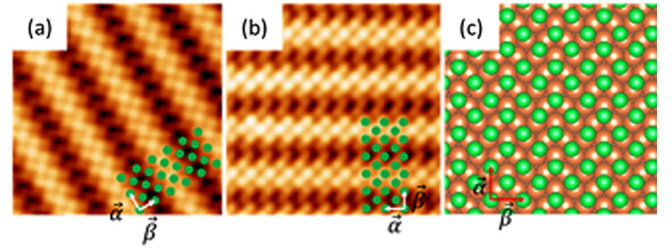


FIG. 3. Atomic structure of the stripe structure. Atom-resolved STM images taken at (a) 0.7 ML ($V = 2.9 \text{ mV}$, $I = 1.0 \text{ nA}$) and (b) 0.8 ML ($V = 5.0 \text{ mV}$, $I = 1.0 \text{ nA}$). The size of each image is $5.6 \times 5.6 \text{ nm}^2$. Green spheres in (a) and (b) indicate the atomic arrangements of Bi. (c) Model of the $(p \times \sqrt{3})$ structure at 0.7 ML ($p = 1.67$). Orange and green spheres represent Au and Bi atoms, respectively. $\vec{\alpha}$ and $\vec{\beta}$ are the unit vectors of the $(p \times \sqrt{3})$ structure (see text for details).

in Figs. 3(a) and 3(b). The detailed structural model for 0.7 ML is shown in Fig. 3(c). In these models, Bi atoms form a rectangular unit cell for which unit vectors are $\vec{\alpha}$ and $\vec{\beta}$. The length of $\vec{\alpha}$ is $\sqrt{3}$ times larger than that of the unit vector of the Au(111) lattice, and remains unchanged with θ . The length of $\vec{\beta}$ decreases as θ increases as determined above. The STM images shown in Figs. 3(a) and 3(b) correspond to the $(1.67 \times \sqrt{3})$ and $(1.63 \times \sqrt{3})$ structures, respectively. These results are consistent with those reported in the previous study [29].

The structure variation of Bi on Au(111) has been investigated in the aqueous condition so far [29,36–38]. Electrochemically deposited Bi atoms form (2×2) and $(p \times \sqrt{3})$ ordered structures. In the present study, a $(p \times \sqrt{3})$ structure is formed for $\theta > 0.7 \text{ ML}$, consistent with the results in the aqueous condition. In contrast, the (2×2) structure is not formed in the UHV condition. This is a notable difference between the aqueous and UHV conditions.

B. Geometric and electronic structures of $\theta > 1.0 \text{ ML}$

Figure 4(a) shows a bird's-eye view of the wide-area STM image for $\theta \sim 2.4 \text{ ML}$. We measured the STM images at locations marked by A–F in the terraces in the STM image. The STM images taken at A–F are shown in Fig. 4(b) together with the atom-resolved images. Image A shows a stripe structure with a rectangular lattice in the atom-resolved image. These features indicate that the stripe structure is the $(p \times \sqrt{3})$ structure which is observed for $\theta \leq 1.0 \text{ ML}$. In the STM images taken at B–F, various superstructures appear with long-range periodicities that are not observed for $\theta \leq 1 \text{ ML}$. The atom-resolved images show that Bi atoms form rectangular lattices. The lattice constants of rectangular lattices for B–F range between $0.457 \sim 0.474 \text{ nm}$ and $0.484 \sim 0.497 \text{ nm}$, which are close to the lattice constants of the bulk Bi(110) surface (0.454 and 0.475 nm) [39]. This indicates that the Bi(110) films grow on the Au(111) surface. The slight differences from the bulk values come from the interface interactions with the hexagonal lattice of Au(111). The main contributors to the interactions are the difference in symmetry between the Bi(110) and Au(111) surfaces as well as the differences in their lattice constants. Table I summarizes the

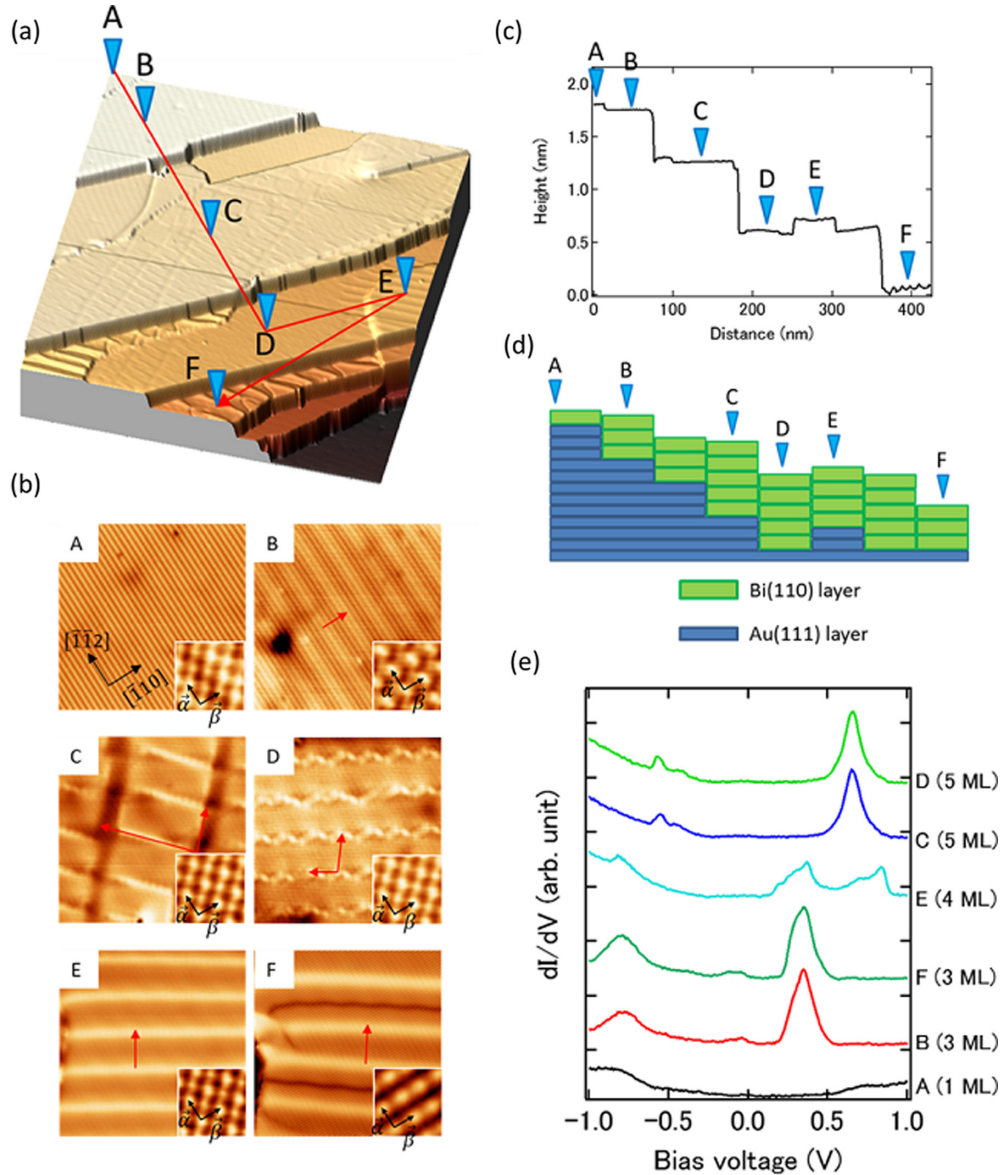


FIG. 4. STM images and dI/dV spectra taken after 2.4 ML deposition. (a) Bird's-eye view of the STM image ($224 \times 224 \text{ nm}^2$, $V = -500 \text{ mV}$, $I = 1.0 \text{ nA}$). (b) High-resolution images ($34 \times 34 \text{ nm}^2$, $V = -500 \text{ mV}$, $I = 1.0 \text{ nA}$) of the regions marked by A–F in (a). The insets show atom-resolved images ($1.4 \times 1.4 \text{ nm}^2$, $V = -10 \text{ mV}$, $I = 1.0 \text{ nA}$) of regions A–F. Crystallographic orientations of the Au(111) substrate are shown in image A and are common in images B–F. Red arrows in B–F indicate the unit vector of long-range patterns. (c) Line profile along the red arrow in (a). (d) Schematic model of the sectional view along the red line in (a). (e) dI/dV spectra measured at regions A–F in (a).

periodicity of the superstructures and the lattice constants of the rectangular lattices.

The superstructures observed at A–F are rationalized as the moiré structures. Superstructure A is reproduced by the superposition of the Bi single layer and the Au surface underneath. Superstructure B can be explained by the moiré structure formed by the combination of two Bi layers and the Au surface. Superstructures C–F are reproduced as moiré structures formed by the superposition of two Bi layers. Table I lists the lattice parameters of the layers used to reproduce the superstructures. The parameters of the first layer are determined from the STM images. A detailed explanation is given in the Appendix.

Figure 4(c) shows a line profile of the red line running from region A to region F in Fig. 4(a). As the $(p \times \sqrt{3})$ structure grows at region A, region A is identified to be the single Bi layer. The height difference along the red line can be rationalized as follows. The height of each terrace is described as $h = h_{\text{Au}}n_{\text{Au}} + h_{\text{Bi}}n_{\text{Bi}}$, where h_{Au} (h_{Bi}) is the thickness of the Au (Bi) single layer and n_{Au} (n_{Bi}) the number of Au (Bi) layers. We use $h_{\text{Au}} = 0.235 \text{ nm}$ and $h_{\text{Bi}} = 0.328 \text{ nm}$. This analysis enables us to determine how many Bi layers stack in each terrace, and we construct a sectional model along the line as shown in Fig. 4(d). We deduce from the sectional model that Bi(110) films of one to five atomic layers grow on the substrate.

TABLE I. Lattice parameters of the moiré structures together with those of the first and second Bi layers. The lattice parameters of the moiré structures and the first Bi layer are determined from the STM images, and those of the second Bi layer are obtained from the moiré analysis (see Appendix). The angles of lattice vectors are measured with respect to the $[110]$ direction of Au(111).

Region	Moiré pattern		First layer		Second layer	
	Lattice constant (nm)	Angle (deg)	Lattice constant (± 0.008 nm)	Angle (deg)	Periodicity (nm)	Angle (deg)
A	1	0	0.463	0		
			0.501	90		
B	1	0	0.459	0	0.423	0
	4.8	0	0.497	90	0.501	90
C	8.5	50	0.464	0	0.468	1.7
	16	135	0.484	90	0.489	88.4
D	7.3	55	0.478	0	0.457	1.2
	5.9	155	0.493	90	0.521	90.4
E	6.8	60	0.457	0	0.441	0
			0.494	90	0.494	93.3
F	7.3	50	0.469	0	0.450	0
			0.489	90	0.489	92.7

We have found that the number of Bi layers correlates with the electronic structure. The dI/dV spectra taken at regions A–F are shown in Fig. 4(e). The spectrum at region A (1 ML) does not show any characteristic features. In contrast, the spectra measured at regions B and F (three layers) exhibit peaks at -780 , -60 , and 350 mV. The spectrum measured at region E (four layers) exhibits peaks at -820 , 470 , and 840 mV and the spectra at C and D (five layers) exhibit peaks at -570 and 660 mV. The dI/dV spectra show that the electronic density of states strongly relates to the number of layers. The previous STM study reports the quantum well states arising from the confinement of electrons in the Bi(110) thin films grown on highly ordered pyrolytic graphite (HOPG) [40]. The spectral features are different from those observed in the present study. The density of states is low for HOPG around the Fermi level due to its semimetallic nature, so the potential barrier at the interface at the Bi layer and HOPG prevents the Bi electrons from propagating into the HOPG and confines the Bi electrons. In contrast, the Au substrate has sp band dispersing around the Fermi level which couples with the Bi electrons. In addition, a wetting layer at the Bi-HOPG interface isolates the Bi layers from the HOPG, while such a wetting layer is not observed on Au(111). Consequently, the confinement in the vertical direction hardly occurs on Au(111) and the electronic structure of the Bi layers is also partially modified, leading to the spectral difference. Furthermore, the in-plane quantum size effect in the narrower terraces of Bi films on HOPG can contribute to the spectral difference. At the current stage, the origin of the thickness-dependent spectral variation as well as the difference from the previous STM study are not fully understood, but it would be extremely interesting to clarify these points.

Figures 5(a) and 5(b) show the STM images of the 60 ML Bi on Au(111). The long-range superstructures observed at $\theta \sim 2.4$ ML disappear. Similarly to the Bi layers shown in Fig. 4, the surface consists of a rectangular unit cell with size 0.46×0.48 nm² [see Fig. 5(b)]. The cell size is almost identical to that of the bulk Bi(110) surface. Figure 5(c) is a line profile along the green arrow in Fig. 5(a). The step height of 0.33 nm agrees with the interlayer spacing of Bi(110) (0.328 nm) [39]. These results indicate that the Bi(110) film of 60 ML

is successfully grown on the Au(111) surface. The stability of thick Bi(110) films can be attributed to the interface relaxation. The analysis about the moiré superstructures indicates that the unit cells of both the Au(111) surface and the Bi(110) layers are relaxed from those of the bulk crystal structures. Several Bi layers at the interface work as buffer layers, stabilize the Bi(110) films, and prevent the transformation of Bi(110) to Bi(111).

We have found that heating causes a structural transition of the Bi(110) films to Bi(111). Figures 5(e) and 5(f) are the STM images of the 60 ML Bi films on Au(111) after annealing at 470 K. One can see that the atomic arrangement drastically changes by heating. As shown in Fig. 5(e), the square lattice converts to a trigonal lattice with a unit cell of size 0.46×0.46 nm². The symmetry and size of the unit cell agree with those of Bi(111) (0.454×0.454 nm²) [39]. Not only the surface lattice but also the step height changes by heating [Fig. 5(g)]. The step height changes from 0.33 to 0.39 nm, which agrees with the layer spacing of Bi(111) (0.394 nm) [39]. Since this structural transition is irreversible, the Bi(110) film is kinetically stable while Bi(111) is the most stable phase of Bi on Au(111).

The structural transition from Bi(110) to Bi(111) is also supported from the spectroscopic viewpoint. The dI/dV spectrum in Fig. 5(d) shows two peaks at 170 and 230 mV. The spectrum in Fig. 5(h) shows a peak at 220 mV and a hump extending from -200 to 50 mV. According to previous angle-resolved photoelectron spectroscopy studies and DFT calculations performed for the bulk Bi(110) surface [41–43], the two spin-split bands locate around 200 meV above the Fermi level. Two peaks observed in Fig. 5(d) match these results and thus provide spectral signatures of Bi(110). In contrast to Bi(110), the electronic structure of Bi(111) has been extensively investigated [43–47]. The peak at 220 mV is assigned to the top of the SOI-split surface states of Bi(111) and the hump corresponds to the bottom of the surface states. Thus, the spectral variation provides spectroscopic evidence of the structure transition from Bi(110) to Bi(111).

It is difficult to grow thick Bi(110) films at RT. The growth of a single Bi(110) layer is reported on Ge(111)

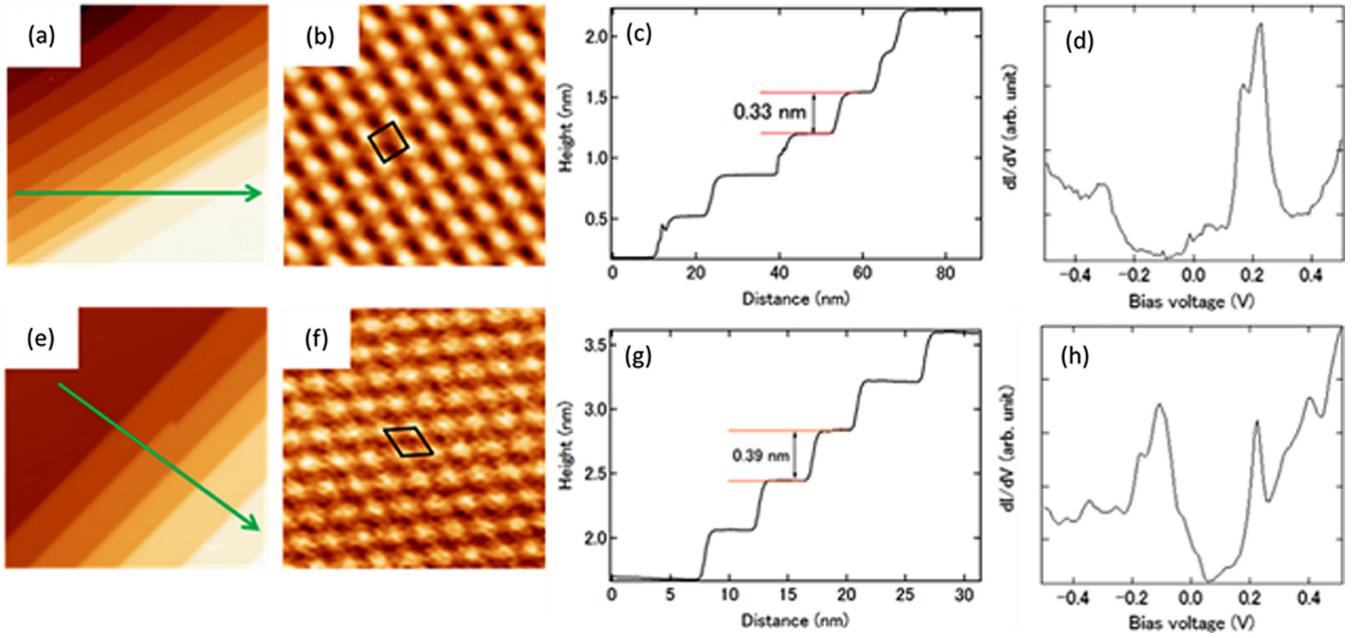


FIG. 5. (a) STM image taken at 60 ML ($112 \times 112 \text{ nm}^2$, $V = 200 \text{ mV}$, $I = 1.0 \text{ nA}$). (b) Atom-resolved STM image taken at the terrace in (a) ($4.0 \times 4.0 \text{ nm}^2$, $V = 100 \text{ mV}$, $I = 1.0 \text{ nA}$). The rectangle indicates the unit cell. (c) Line profile along the green arrow in (a). (d) dI/dV spectrum taken at the terrace of (a). (e) STM image taken after heating the 60 ML Bi films on Au(111) at 470 K ($34 \times 34 \text{ nm}^2$, $V = 500 \text{ mV}$, $I = 1.0 \text{ nA}$). (f) Atom-resolved STM image taken at the terrace in (e) ($4.0 \times 4.0 \text{ nm}^2$, $V = 100 \text{ mV}$, $I = 1.0 \text{ nA}$). The rhombus indicates the unit cell. (g) Line profile along the green arrow in (d). (h) dI/dV spectrum taken at the terrace of (e).

[20], Si(111) ($\sqrt{3} \times \sqrt{3}$)-Bi [19] and Si(111) ($\sqrt{3} \times \sqrt{3}$)-B [48], but the layer converts to a Bi(111) film with increasing thickness. The deposition of Bi on the substrates kept at low temperature has been performed, but the grown Bi(110) films are polycrystalline and not stable at RT [49,50]. Very recently, thick Bi(110) films deposited on Al_2O_3 at low temperature were found to be stable above room temperature [51]. To the best of our knowledge, this is the only example other than the present study that realizes the growth of thick Bi(110) films. The growth of thick Bi(110) films on two substrates whose electronic structures are different from each other offers a unique opportunity for further investigation of novel electronic properties of Bi(110). The Au(111) substrate is metallic and adequate for studying electronic structure using electron spectroscopies and scanning tunneling spectroscopy,

while insulating Al_2O_3 is useful for transport measurements. Proper selection of the substrate would help us gain a better understanding of Bi(110).

Finally, we compare the structural variation of Bi on Au(111) and Ag(111). For the deposition of Bi on Ag(111), the surface alloy of Ag_2Bi grows in areas of low coverage, and the ($\sqrt{3} \times \sqrt{3}$) structure forms at 1/3 ML [1,25,26]. Increasing the coverage, dealloying occurs and stripe structures of ($p \times \sqrt{3}$) appear similarly to Bi on Au(111) [25,26]. In coverage of more than 1 ML, anisotropic Bi(110) bilayer ribbons grow [52]. Although the anisotropic growth of Bi layers is not observed on Au(111) at a few-ML regime [see Fig. 4(a)], the Bi(110) layers grow anisotropically at much larger coverages. Figure 6(a) shows an STM image taken at 12 ML. In the high-resolution STM image in the inset of Fig. 6(a), the

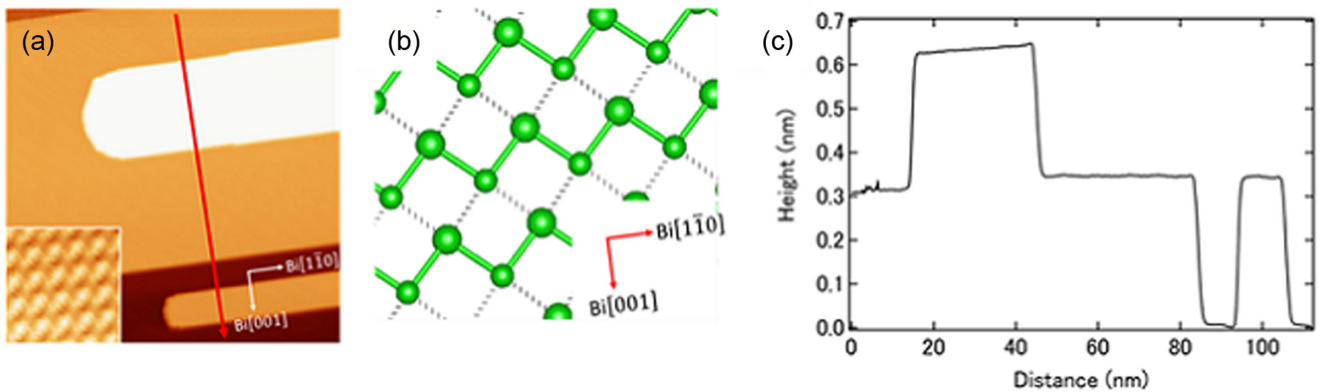


FIG. 6. (a) STM image taken at 12 ML Bi on Au(111) ($112 \times 112 \text{ nm}^2$, $V = -300 \text{ mV}$, $I = 0.5 \text{ nA}$). Inset is atomic-resolution STM image ($2.3 \times 2.3 \text{ nm}^2$, $V = -300 \text{ mV}$, $I = 0.8 \text{ nA}$). (b) Schematic illustration of atomic structure of Bi(110). The spheres represent Bi atoms. (c) Line profile along the red arrow in (a).

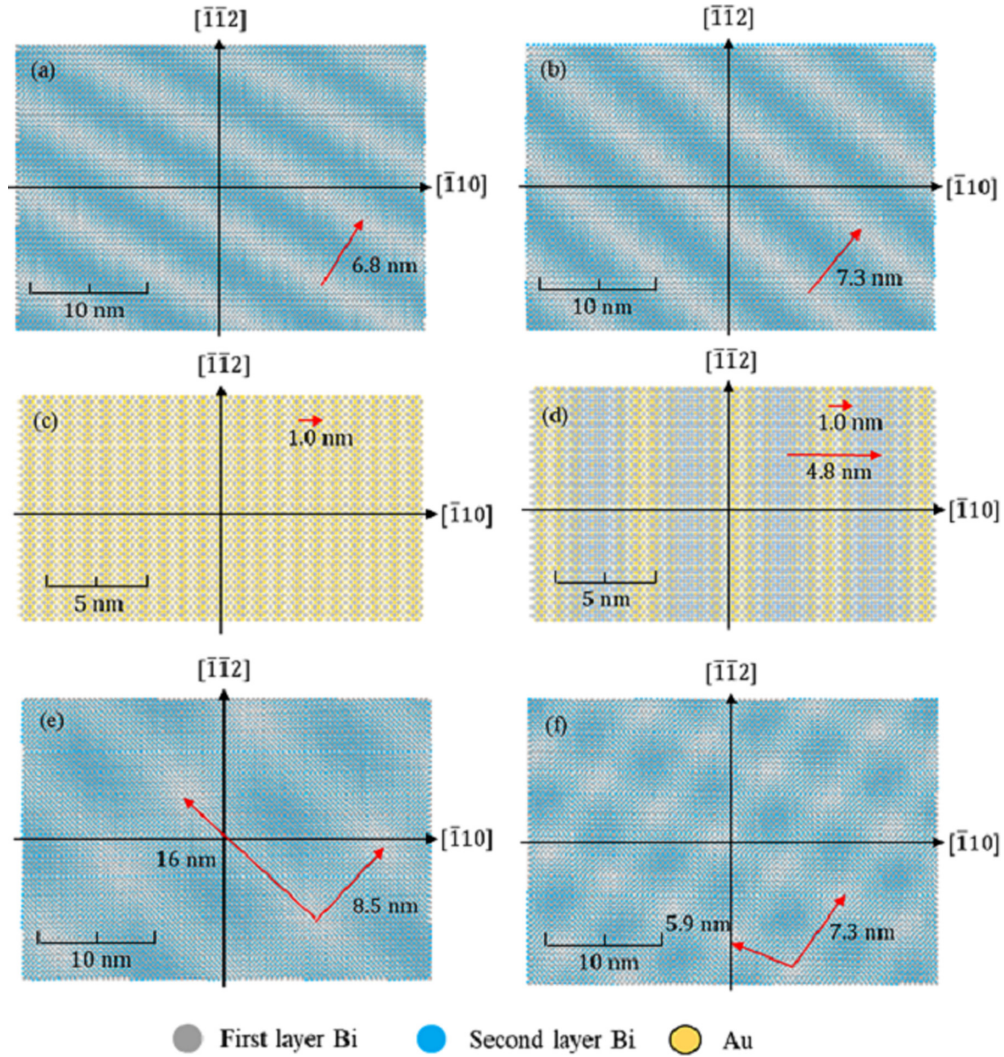


FIG. 7. Structural models of the moiré patterns observed in the STM experiments. The gray and blue spheres represent the Bi atoms in the first and second layer, respectively. The yellow spheres in (a) and (b) represent the Au atoms. (a), (b), (c), (d), (e), and (f) correspond to superstructures A, B, E, F, C, and D, respectively. $[\bar{1}10]$ and $[\bar{1}\bar{1}2]$ indicate the directions with respect to the Au(111) substrate. The red arrows indicate the unit vectors of moiré patterns.

rectangular lattice of the Bi(110) surface appears. Comparing the STM image with the structural model of Bi(110) in Fig. 6(b), the Bi(110) island grows in the Bi $[\bar{1}\bar{1}0]$ direction, which is similar to the bilayer Bi(110) ribbons on Ag(111). Figure 6(c) exhibits the line profile along the arrow in Fig. 6(a). The height difference is 0.32 nm, coinciding with the single step height of Bi(110). The single-step growth is markedly different from the bilayer growth on Ag(111) [52]. Although the lattice constants of Au(111) and Ag(111) are very similar, the structural evolutions on two substrates are different from each other except for the formation of the $(p \times \sqrt{3})$ structure. Further investigation of these differences would promote our understanding of surface physics and chemistry relevant to the adsorption of Bi on solid surfaces as well as material synthesis on solid surfaces.

IV. SUMMARY

The structural evolution of Bi on Au(111) was investigated mainly by using STM. We have found three phases

for $\theta < 1$ ML: the cluster array with (5×5) periodicity, and $(\sqrt{37} \times \sqrt{37})R25.3^\circ$ and $(p \times \sqrt{3})$ structures. We have revealed that the structure reported previously as $p(6 \times 6)$ should be the $(\sqrt{37} \times \sqrt{37})R25.3^\circ$ structure and proposed the structural model. Above 1 ML, the Bi(110) films form and grow stably above 60 ML. The dI/dV spectra of Bi films reveal that the electronic structure correlates with the layer number. The structural transition from Bi(110) to Bi(111) occurs by heating at 470 K. It is difficult to realize the thick Bi(110) films and thus the present system would provide a proper stage for investigating the peculiar electronic characteristics of Bi(110).

ACKNOWLEDGMENTS

This work was partially supported by Grants-in-aid for Scientific research from Ministry of Education, Culture, Sports, Science and Technology (MEXT), Japan (Grant No. 25110008). The DFT calculations were performed by using the computer facilities of the Institute of Solid State Physics (ISSP Super Computer Center, University of Tokyo) and the

National Institute for Materials Science (Numerical Material Simulator).

APPENDIX

As shown in Fig. 4, various superstructures emerge that are more than 1 ML. In this Appendix, we demonstrate that moiré structures explain these superstructures. While there are several methods for considering moiré structure [53–57], it is straightforward to consider in reciprocal space how a moiré structure forms from two overlapping layers [53–55]. Let the reciprocal lattice vectors that specify the i th layer ($i = 1, 2$) be \vec{a}_i^* and \vec{b}_i^* , and those for the moiré be \vec{m}^* and \vec{n}^* . In addition, we set $\vec{a}_{21}^* = \vec{a}_2^* - \vec{a}_1^*$ and $\vec{b}_{21}^* = \vec{b}_2^* - \vec{b}_1^*$. \vec{m}^* and \vec{n}^* are described as linear combinations of \vec{a}_{21}^* and \vec{b}_{21}^* as follows:

$$\begin{pmatrix} \vec{m}^* \\ \vec{n}^* \end{pmatrix} = K \begin{pmatrix} \vec{a}_{21}^* \\ \vec{b}_{21}^* \end{pmatrix}, \quad (\text{A1})$$

where K is a 2×2 matrix whose components are integers. We apply Eq. (A1) for the analysis of each superstructure. First, we specify the matrix K . Then, we calculate \vec{a}_2^* and \vec{b}_2^* as well as the corresponding lattice vectors in real space by using Eq. (A1) with \vec{m}^* , \vec{n}^* , \vec{a}_1^* , and \vec{b}_1^* , which are determined experimentally from the STM images. Finally, we judge whether the calculated \vec{a}_2^* and \vec{b}_2^* are reasonable.

The simplest case is provided by $K = \begin{bmatrix} 1 & 0 \\ 0 & 1 \end{bmatrix}$. We call this type of moiré a first-order moiré. The superstructures A, B, E, and F exhibit one-dimensional periodicity ($\vec{n}^* = 0$) and can be explained by the first-order moiré. By using Eq. (A1) with \vec{m}^* , \vec{a}_1^* , and \vec{b}_1^* determined from the STM images, we have determined the lattice parameters of the second layer as shown

in Table I. Superstructure A is reproduced by overlapping a Bi layer on Au stretched about 10% along the $[\bar{1}10]$ direction. Superstructure B is characterized by two types of stripe. One type of stripe is arranged with an interstripe distance of 4.8 nm and the other with a distance of 1 nm. Three layers are required to explain these distances. The former is reproduced by stacking two Bi layers and the latter the superposition of the Bi layer and the Au surface. Similarly to superstructure A, the Au lattice is stretched along the $[\bar{1}10]$ direction. Superstructures E and F are rationalized by the superposition of two Bi layers. In superstructure E, the shorter side of the unit cell in the second Bi layer reduces by 3.4% and the longer side slightly tilts 3.3° with respect to the first Bi layer. The unit cell of the second layer is oblique while that of the first layer is rectangular. In superstructure F, the shorter side of the unit cell reduces by 4.1% and the longer side tilts 2.7° . The structural models of superstructures A, B, E, and F are shown in Figs. 7(a)–7(d), respectively. These superstructures are successfully reproduced.

Next, we consider the case of $K = \begin{bmatrix} 1 & 1 \\ 1 & -1 \end{bmatrix}$. We call this type of moiré a second-order moiré. We find that superstructures C and D are well explained as the second-order moiré formed by the superposition of two Bi layers. As shown in Table I, the lattice parameters determined for the second layer are slightly changed from those of the first layer. The differences in the lattice constants are 6% at most. The structural models for C and D are shown in Figs. 7(e) and 7(f), respectively. Two superstructures observed by STM are well reproduced and their periodicities are consistent with the experimental data. Then, we have succeeded in reproducing the six superstructures shown in Fig. 4 by using the moiré pattern between Bi(110) layers or Bi(110) and the Au lattice.

-
- [1] C. R. Ast, J. Henk, A. Ernst, L. Moreschini, M. C. Falub, D. Pacilé, P. Bruno, K. Kern, and M. Grioni, *Phys. Rev. Lett.* **98**, 186807 (2007).
 - [2] L. Moreschini, A. Bendounan, H. Bentmann, M. Assig, K. Kern, F. Reinert, J. Henk, C. R. Ast, and M. Grioni, *Phys. Rev. B* **80**, 035438 (2009).
 - [3] S. Murakami, *Phys. Rev. Lett.* **97**, 236805 (2006).
 - [4] Y. Lu, W. Xu, M. Zeng, G. Yao, L. Shen, M. Yang, Z. Luo, F. Pan, K. Wu, T. Das, P. He, J. Jiang, J. Martin, Y. P. Feng, H. Lin, and X. Wang, *Nano Lett.* **15**, 80 (2015).
 - [5] T. Hirahara, G. Bihlmayer, Y. Sakamoto, M. Yamada, H. Miyazaki, S. I. Kimura, S. Blügel, and S. Hasegawa, *Phys. Rev. Lett.* **107**, 166801 (2011).
 - [6] F. Yang, L. Miao, Z. F. Wang, M.-Y. Yao, F. Zhu, Y. R. Song, M.-X. Wang, J.-P. Xu, A. V. Fedorov, Z. Sun, G. B. Zhang, C. Liu, F. Liu, D. Qian, C. L. Gao, and J.-F. Jia, *Phys. Rev. Lett.* **109**, 016801 (2012).
 - [7] S. H. Kim, K.-H. Jin, J. Park, J. S. Kim, S.-H. Jhi, T.-H. Kim, and H. W. Yeom, *Phys. Rev. B* **89**, 155436 (2014).
 - [8] I. K. Drozdov, A. Alexandradinata, S. Jeon, S. Nadj-Perge, H. Ji, R. J. Cava, B. A. Bernevig, and A. Yazdani, *Nat. Phys.* **10**, 664 (2014).
 - [9] N. Kawakami, C.-L. Lin, M. Kawai, R. Arafune, and N. Takagi, *Appl. Phys. Lett.* **107**, 031602 (2015).
 - [10] A. Takayama, T. Sato, S. Souma, T. Oguchi, and T. Takahashi, *Phys. Rev. Lett.* **114**, 066402 (2015).
 - [11] H. W. Yeom, K.-H. Jin, and S.-H. Jhi, *Phys. Rev. B* **93**, 075435 (2016).
 - [12] M. Wada, S. Murakami, F. Freimuth, and G. Bihlmayer, *Phys. Rev. B* **83**, 121310 (2011).
 - [13] G. Bian, X. Wang, T. Miller, T.-C. Chiang, P. J. Kowalczyk, O. Mahapatra, and S. A. Brown, *Phys. Rev. B* **90**, 195409 (2014).
 - [14] K. Tamura, B. M. Ocko, J. X. Wang, and R. R. Adžić, *J. Phys. Chem. B* **106**, 3896 (2002).
 - [15] M. Nakamura, N. Sato, N. Hoshi, and O. Sakata, *Langmuir* **26**, 4590 (2010).
 - [16] M. Hara, Y. Nagahara, S. Yoshimoto, J. Inukai, and K. Itaya, *Jpn. J. Appl. Phys.* **43**, 7232 (2004).
 - [17] J. Wu, Y. Miao, X. Liang, Z. Yang, Y. Yang, and R. Ouyang, *Electroanalysis* **26**, 856 (2014).
 - [18] T. Nagao, J. T. Sadowski, M. Saito, S. Yaginuma, Y. Fujikawa, T. Kogure, T. Ohno, Y. Hasegawa, S. Hasegawa, and T. Sakurai, *Phys. Rev. Lett.* **93**, 105501 (2004).
 - [19] S. Yaginuma, T. Nagao, J. T. Sadowski, M. Saito, K. Nagaoka, Y. Fujikawa, T. Sakurai, and T. Nakayama, *Surf. Sci.* **601**, 3593 (2007).
 - [20] S. Hattai, Y. Ohtsubo, S. Miyamoto, H. Okuyama, and T. Aruga, *Appl. Surf. Sci.* **256**, 1252 (2009).

- [21] M. Yokoyama, W. S. Liang, W. Chen, A. T. S. Wee, T. Matsui, and J. Yuhara, *Surf. Sci.* **605**, 844 (2011).
- [22] S. A. Scott, M. V. Kral, and S. A. Brown, *Surf. Sci.* **587**, 175 (2005).
- [23] D. Kaminski, P. Poodt, E. Aret, N. Radenovic, and E. Vlieg, *Surf. Sci.* **575**, 233 (2005).
- [24] Y. Girard, C. Chacon, C. de Abreu, J. Lagoute, V. Repain, and S. Rousset, *Surf. Sci.* **617**, 118 (2013).
- [25] C. Kato, Y. Aoki, and H. Hirayama, *Phys. Rev. B* **82**, 165407 (2010).
- [26] K. H. L. Zhang, I. M. McLeod, Y. H. Lu, V. R. Dhanak, A. Matilainen, M. Lahti, K. Pussi, R. G. Egde, X.-S. Wang, A. T. S. Wee, and W. Chen, *Phys. Rev. B* **83**, 235418 (2011).
- [27] S. Mathias, A. Ruffing, F. Deicke, M. Wiesenmayer, I. Sakar, G. Bihlmayer, E. V. Chulkov, Yu. M. Koroteev, P. M. Echenique, M. Bauer, and M. Aeschlimann, *Phys. Rev. Lett.* **104**, 066802 (2010).
- [28] J. H. Jeon, K. H. Chung, H. Kim, and S. Kahng, *Surf. Sci.* **603**, 145 (2009).
- [29] C. Chen, K. D. Kepler, A. A. Gewirth, B. M. Ocko, and J. Wang, *J. Phys. Chem.* **97**, 7290 (1993).
- [30] G. Kresse and J. Furthmüller, *Phys. Rev. B* **54**, 11169 (1996).
- [31] G. Kresse and J. Furthmüller, *Comput. Mater. Sci.* **6**, 15 (1996).
- [32] P. E. Blöchl, *Phys. Rev. B* **50**, 17953 (1994).
- [33] J. P. Perdew, K. Burke, and M. Ernzerhof, *Phys. Rev. Lett.* **77**, 3865 (1996).
- [34] D. Hobbs, G. Kresse, and J. Hafner, *Phys. Rev. B* **62**, 11556 (2000).
- [35] I. Horcas, R. Fernández, J. M. Gómez-Rodríguez, J. Colchero, J. Gómez-Herrero, and A. M. Baro, *Rev. Sci. Instrum.* **78**, 013705 (2007).
- [36] C. A. Jeffrey, D. A. Harrington, and S. Morin, *Surf. Sci.* **512**, L367 (2002).
- [37] C. A. Jeffrey, S. H. Zheng, E. Bohannon, D. A. Harrington, and S. Morin, *Surf. Sci.* **600**, 95 (2006).
- [38] H. Matsushima, S.-W. Lin, S. Morin, and O. M. Magnussen, *Faraday Discuss.* **193**, 171 (2016).
- [39] Ph. Hofmann, *Prog. Surf. Sci.* **81**, 191 (2006).
- [40] P. J. Kowalczyk, O. Mahapatra, S. A. Brown, G. Bian, X. Wang, and T.-C. Chiang, *Nano Lett.* **13**, 43 (2013).
- [41] S. Agergaard, Ch. Søndergaard, H. Li, M. B. Nielsen, S. V. Hoffmann, Z. Li, and Ph. Hofmann, *New J. Phys.* **3**, 15 (2001).
- [42] J. I. Pascual, G. Bihlmayer, Yu. M. Koroteev, H.-P. Rust, G. Ceballos, M. Hansmann, K. Horn, E. V. Chulkov, S. Blügel, P. M. Echenique, and Ph. Hofmann, *Phys. Rev. Lett.* **93**, 196802 (2004).
- [43] Yu. M. Koroteev, G. Bihlmayer, J. E. Gayone, E. V. Chulkov, S. Blügel, P. M. Echenique, and Ph. Hofmann, *Phys. Rev. Lett.* **93**, 046403 (2004).
- [44] T. Hirahara, K. Miyamoto, I. Matsuda, T. Kadono, A. Kimura, T. Nagao, G. Bihlmayer, E. V. Chulkov, S. Qiao, K. Shimada, H. Namatame, M. Taniguchi, and S. Hasegawa, *Phys. Rev. B* **76**, 153305 (2007).
- [45] T. Hirahara, T. Nagao, I. Matsuda, G. Bihlmayer, E. V. Chulkov, Yu. M. Koroteev, P. M. Echenique, M. Saito, and S. Hasegawa, *Phys. Rev. Lett.* **97**, 146803 (2006).
- [46] S. Yaginuma, K. Nagaoka, T. Nagao, G. Bihlmayer, Yu. M. Koroteev, E. V. Chulkov, and T. Nakayama, *J. Phys. Soc. Jpn.* **77**, 014701 (2008).
- [47] M. C. Cottin, C. A. Bobisch, J. Schaffert, G. Inawali, G. Bihlmayer, and R. Möller, *Nano Lett.* **13**, 2717 (2013).
- [48] I. Kokubo, Y. Yoshiike, K. Nakatsuji, and H. Hirayama, *Phys. Rev. B* **91**, 075429 (2015).
- [49] K. S. Wu and M. Y. Chern, *J. Appl. Phys.* **104**, 033704 (2008).
- [50] D. N. McCarthy, S. Yaginuma, H. Gui, and T. Nagao, *CrystEngComm* **13**, 4604 (2011).
- [51] M. Jankowski, D. Kamiński, K. Vergeer, M. Mirolo, F. Carla, G. Rijnders, and T. R. J. Bollmann, *Nanotechnology* **28**, 155602 (2017).
- [52] H. L. Zhang, W. Chen, X. S. Wang, J. Yuhara, and A. T. S. Wee, *Appl. Surf. Sci.* **256**, 460 (2009).
- [53] P. Zeller, X. Ma, and S. Günther, *New J. Phys.* **19**, 013015 (2017).
- [54] P. Zeller and S. Günther, *New J. Phys.* **16**, 083028 (2014).
- [55] K. Hermann, *J. Phys.: Condens. Matter* **24**, 314210 (2012).
- [56] K. Kawahara, R. Arafune, M. Kawai, and N. Takagi, *e-J. Surf. Sci. Nanotechnol.* **13**, 361 (2015).
- [57] B. Wang and M.-L. Bocquet, *J. Phys. Chem. Lett.* **2**, 2341 (2011).